

## Direct numerical simulation of flapping flags in grid-induced turbulence

Stefano Olivieri,<sup>1</sup> Francesco Viola,<sup>2</sup> Andrea Mazzino,<sup>3,4</sup> and Marco E. Rosti<sup>1</sup>

<sup>1</sup>*Complex Fluids and Flows Unit, Okinawa Institute of Science and Technology Graduate University, 1919-1 Tancha, Onna-son, Okinawa 904-0495, Japan*<sup>a)</sup>

<sup>2</sup>*Gran Sasso Science Institute, Viale F. Crispi 7, 67100, L'Aquila, Italy*

<sup>3</sup>*Department of Civil, Chemical and Environmental Engineering (DICCA), University of Genova, Via Montallegro 1, 16145 Genova, Italy*

<sup>4</sup>*INFN, Genova Section, Via Montallegro 1, 16145 Genova, Italy*

(Dated: 1 March 2025)

A fully-resolved DNS approach for investigating flexible bodies invested by a turbulent incoming flow is designed to study the flapping motion of a flexible flag at moderate Reynolds number. The incoming turbulent flow is generated by placing a passive grid at the inlet of the numerical domain and the turbulence level of the flow investing the flag can be controlled by changing its downstream distance from the grid. The computational framework is based on the immersed boundary method for dealing with arbitrary geometries and implemented using a GPU-accelerated parallelisation to increase the computational efficiency. The grid-induced turbulent flow is first characterised by means of the comparison with well-known results for decaying turbulence and a scale-by-scale analysis. Then, the flag-in-the-wind problem is revisited by exploring the effect of the turbulence intensity on self-sustained flapping. Whilst the latter is still manifesting under strong fluctuations, the main features of the oscillation (including its amplitude and frequency) are altered by turbulence, whose fingerprint can also be qualitatively detected by spectral analysis. Besides their relevance for advancing the fundamental understanding of fluid-structure interaction in turbulence, these findings have potential impact for related applications, e.g., aeroelastic energy harvesting or flow control techniques.

---

<sup>a)</sup>Corresponding author: stefano.olivieri@oist.jp

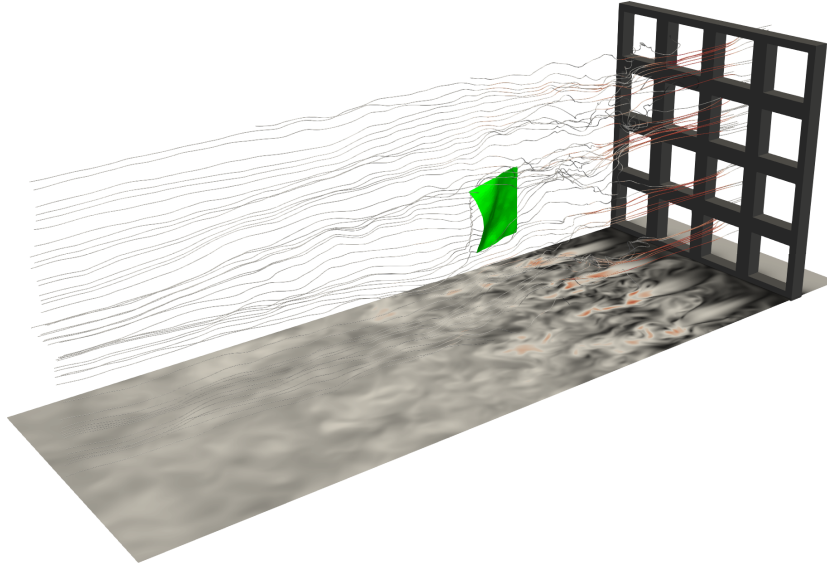


FIG. 1. Fluid-structure interaction between a flexible flag (green) and the turbulent flow generated using a passive grid (gray). Snapshot from DNS where the instantaneous fluid flow is shown by means of streamlines in the domain and contours onto a longitudinal plane (normal to the transverse direction), both coloured (from black to red) by the fluid velocity magnitude. The flag is hinged at its leading edge while the other edges are free to move.

## I. INTRODUCTION

Fluid-structure interaction (FSI) is ubiquitous and governs many physical problems with relevance in natural processes<sup>1-3</sup> and engineering applications<sup>4-9</sup>. A formidable and renovated effort has been devoted to understand these problems in more details and, in particular, characterise the aeroelastic instabilities leading to self-sustained, flow-induced oscillations<sup>10-12</sup>. Notwithstanding, the consolidated knowledge is almost exclusively limited to the case where the incoming flow is laminar. Indeed, only a few studies have considered the role of free-stream turbulence in altering the resulting dynamics<sup>13-15</sup>. To fill the gap in the current knowledge, the analysis has therefore to be enriched by considering the typical, yet scarcely explored, configuration where the fluid flow is intrinsically turbulent. In this work, we revisit a well-known FSI problem, i.e. the flapping instability of a flexible flag, in the presence of a turbulent flow generated by using a passive grid (Fig. 1).

Grid-induced turbulence is one of the most typical configurations adopted for experimental fundamental research on turbulent flows<sup>16–18</sup> and many related problems, e.g. mixing processes<sup>19–21</sup> or aerodynamic testing<sup>22,23</sup>. Earliest experimental investigations using such configuration date back to Batchelor and Townsend<sup>24,25</sup>. Since then, numerous studies of both experimental and theoretical nature have focused on various aspects of decaying turbulence, including the existence of self-preserving solutions<sup>16,26</sup> as well as the influence of the so-called initial (i.e., upstream) conditions on the properties of the generated turbulence<sup>27–30</sup>. Although the full validation of a comprehensive theory for decaying turbulence is still a debated topic<sup>31</sup>, it is widely accepted that the turbulent fluctuations decay along the mean flow direction according to a power law that can be expressed (in the laboratory frame of reference) as

$$\langle u_i'^2 \rangle \sim (x - x_0)^{-n}, \quad (1)$$

where  $u_i'$  is the fluctuating part of a generic velocity component,  $(x - x_0)$  is a properly adjusted distance from the grid and  $n$  is the power-law exponent.

While grid-induced turbulence is a standard configuration in the experimental practice, the situation is remarkably different in the computational framework and, in particular, for what it concerns the state of the art of *fully-resolved* (i.e., explicitly modeling the presence of the turbulence-generating grid and its geometrical details), direct numerical simulations (DNSs). Indeed, only a few seminal papers addressed the problem in this perspective<sup>32–37</sup>, while the vast majority of previous studies focused on the simulation of freely-decaying homogeneous turbulence in a triperiodic domain imposing some representative initial fluid flow conditions<sup>38</sup>. The simulation of grid turbulence in such a fully-resolved approach requires a particular effort on the computational side because of (at least) two critical requirements: (i) to appropriately model the initial or upstream conditions (essentially related to the grid geometry), which are known to influence the properties of the resulting turbulent flow<sup>29</sup>; (ii) to consider a very large extension of the computational domain (in particular along the streamwise direction), in order to describe the whole fully-developed range of turbulence decay. While the first issue can be solved using suitable numerical methods, the second represents an unavoidable challenge that has to be faced by means of an efficient high-performance-computing (HPC) strategy.

Among the first investigations of grid-induced turbulence by fully-resolved numerical simulations, Djenidi<sup>32</sup> originally tackled the problem (using a Lattice-Boltzmann method complemented by a LES correction scheme) modeling the grid as an array of floating squares normal to the

incoming flow. Along with highlighting the most delicate aspects in carrying out this kind of computationally-challenging simulation, this study provided a first set of numerical results which are compared with similar experimental measurements. Nagata *et al.*<sup>33</sup> later investigated the turbulent heat transfer considering a thermal mixing layer and investigating several types of grid geometries by means of an immersed boundary method to model the no-slip condition on the grid elements. Using a similar approach, Laizet and Vassilicos<sup>35</sup> and Suzuki *et al.*<sup>36</sup> performed DNS studies on so-called fractal grids, with the goal of characterising the flow obtained using this specific type of geometry and mostly focusing on the production region relatively close to the grid. Overall, these contributions provided valuable knowledge and demonstrated the feasibility of DNS using a fully-resolved approach. Nevertheless, the development and employment of this kind of computational tool is still in its early stage, both for fundamental research and related applications, e.g., in aerodynamics or fluid-structure interaction problems. In particular, the critical aspects limiting the current state of the art are typically represented by the highest Reynolds number and maximum streamwise extension that can be achieved.

In FSI, the effect of turbulence can be crucial on triggering (or suppressing) the onset of aeroelastic instabilities and more generally altering the characteristics of the resulting flow-induced oscillations, thus affecting, e.g., the potential for energy harvesting<sup>9,10,39</sup>. In particular, here we focus on the three-dimensional flapping dynamics of a flexible flag, a problem attracting significant attention both from the fundamental and applied perspective<sup>5,6,12,40,41</sup>, however so far substantially limited to the situation where the incoming flow is laminar. To tackle the problem, we first present an efficient and accurate computational framework for performing fully-resolved DNS of grid turbulence at moderate Reynolds numbers. Then, we revisit the classical flag-in-the-wind problem focusing on the influence of the incoming turbulence, unraveling the main similarities and differences with respect to the laminar case.

The rest of the paper is organised as follows. In Sec. II, we first introduce the governing equations and relevant physical parameters (Sec. II A) and then describe the computational methodology and discuss some technical features (Sec. II B). Sec. III concerns the characterisation of the generated turbulent flow and Sec. IV reports our findings on the flag-in-the-wind problem in the case of incoming turbulent flow. Finally, Sec. V draws some conclusions.

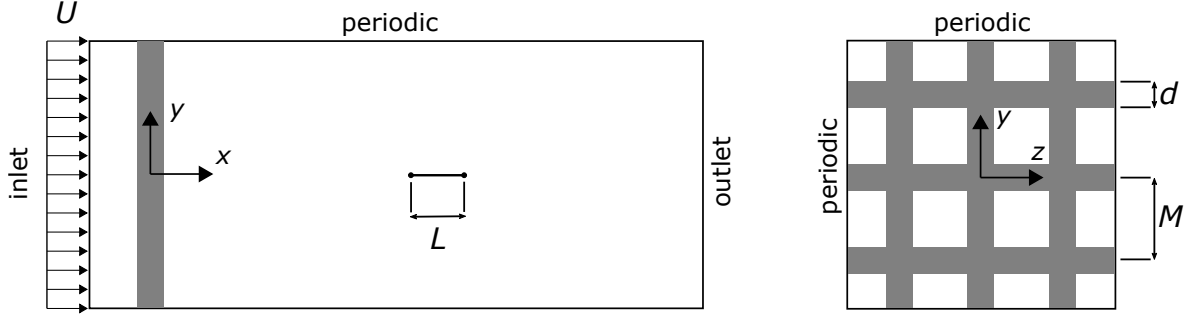


FIG. 2. Sketch of the problem (left: sideview, right: front view). A rectangular fluid domain is considered with inlet/outlet conditions in the streamwise direction  $x$  and periodic boundary conditions along the transverse directions  $y$  and  $z$ . A regular passive grid, characterised by square rods of side  $d$  and spacing  $M$ , is placed close to the inlet (at  $x = 0$ ) to generate the turbulent flow. A flexible flag of side  $L$  (both in the streamwise and spanwise extension) is placed downstream of the grid.

## II. METHODOLOGY

### A. Problem definition

We consider a Newtonian fluid flow governed by the incompressible Navier-Stokes equations:

$$\frac{\partial \mathbf{u}}{\partial t} + \mathbf{u} \cdot \nabla \mathbf{u} = -\nabla p / \rho + \nu \nabla^2 \mathbf{u} + \mathbf{f}, \quad (2)$$

$$\nabla \cdot \mathbf{u} = 0, \quad (3)$$

where  $\mathbf{u} = \mathbf{u}(\mathbf{x}, t)$  is the velocity and  $p = p(\mathbf{x}, t)$  the pressure fields,  $\rho$  and  $\nu$  are the fluid density and kinematic viscosity, respectively, and  $\mathbf{f} = \mathbf{f}(\mathbf{x}, t)$  is a body force mimicking the presence of solid bodies (as later discussed in Sec. II B). The fluid domain is a box of size  $L_x \times L_y \times L_z$  along the streamwise, vertical and spanwise directions, with the origin of the reference frame coinciding with the geometrical centre of the grid used to generate turbulence. A schematic description of the geometrical setup is shown in Fig. 2. A uniform fluid velocity  $\mathbf{u} = (U, 0, 0)$  is imposed at the inlet, whereas a non-reflecting convective boundary condition is used at the outlet. Periodic boundary conditions apply along the vertical and spanwise directions, this setup being representative of the central region of a wind-tunnel sufficiently far from the surrounding walls.

A monoplane, passive grid is placed immediately after the inlet to induce the turbulence, as shown in Fig. 2. The no-slip boundary condition applies at the solid surface of the grid. The grid geometry is characterised by the spacing  $M$  between the elements and by their cross-sectional

shape and size. Here, we consider a square cross section with rod side  $d$ . Note that we choose a monoplane grid, but other configurations could be considered as well, including active grids using appropriate boundary conditions and geometrical elements. The problem is made nondimensional using the grid spacing  $M$  and the unperturbed flow velocity  $U$ , so that we define the nominal Reynolds number  $\text{Re}_M = UM/\nu$  and the geometrical ratio  $M/d$  or, equivalently, the grid porosity  $\alpha = (1 - d/M)^2$  and solidity  $\sigma = 1 - \alpha$ , as the main nondimensional governing parameters. Here, we fix  $M/d = 4$ , or equivalently  $\sigma = 44\%$ , in order to achieve a rather strong turbulence intensity while ensuring a good isotropy<sup>30</sup>. Moreover, such configuration will allow to compare our results with available experimental data from Djenidi, Kamruzzaman, and Antonia<sup>31</sup>.

As a representative FSI, we consider the well-known (three-dimensional) problem of a flag flapping in the wind<sup>40</sup>. A square flag of side  $L$  is placed at a given streamwise distance downstream of the grid (and centered in the middle of the transverse plane). We assume  $L = M$  so that the integral lengthscale of the incoming turbulent flow is strictly comparable with the size of the elastic objects. From this choice it also follows that the flag and grid nominal Reynolds numbers match, i.e.  $\text{Re}_L = UL/\nu = \text{Re}_M = \text{Re}$ . Besides this parameter, in the case of a uniform incoming flow, the flapping dynamics is controlled by the mass ratio  $\rho = (\rho_s/\rho_f)(h/L)$  (where  $\rho_s$  is the solid density and  $h$  is the flag thickness) and the bending coefficient  $\beta = B/(\rho_f U^2 L^3)$ , where  $B$  is the dimensional bending stiffness. In order to compare with available results in the laminar case<sup>40,42–44</sup>, we neglect the presence of gravity and set  $\rho = 1$  and  $\beta = 10^{-4}$ ; the flag is always initialised in the straight configuration with a pitching angle  $\theta = 0.1\pi$  to trigger the flapping instability.

## B. Numerical technique

A critical aspect in the numerical simulation of grid-induced turbulence is represented by the streamwise extension needed to capture the whole dynamical range of interest, i.e., from the production region to that of the final decay<sup>32</sup>. At the same time, the spatial resolution needs to be sufficient to accurately describe the flow features especially in the vicinity of the solid surfaces. The combination of these requirements leads to a dramatic increase in the total number of computational nodes. To tackle such a challenging problem, we employ the recently developed GPU-based parallel version of the AFiD solver<sup>45</sup>. Hereafter, we briefly discuss its main features, while for additional information the reader is referred to Refs.<sup>45–47</sup>.

Eqs. (2) and (3) are solved numerically using the fractional-step method on a regular staggered Eulerian mesh. The spatial discretisation is performed using the second-order centered finite-difference method. The nonlinear terms are discretised in time using the second-order Adams-Bashfort scheme whereas the diffusive terms are computed with the second-order Crank-Nicolson scheme. The no-slip condition on the wet surfaces of the immersed solid bodies is imposed using the immersed boundary (IB) method<sup>44,48</sup>, with the solid bodies discretised onto a non-conformal triangular mesh. A provisional, non-solenoidal velocity field is first computed using an approximate factorization technique and then updated by applying the IB forcing. Then, the provisional velocity is projected onto a divergence-free space after solving the resulting Poisson equation enforcing mass conservation.

Two different types of direct-forcing IB methods are used to enforce the no-slip boundary condition between the fluid and the solid surfaces: *(i)* for the fixed surface of the grid used to generate turbulence, we employ the Eulerian method proposed in Ref.<sup>48</sup>; *(ii)* for the moving surface of the flapping flag, we employ a Lagrangian approach based on a moving-least-squares method<sup>44,49</sup>. Indeed, the first method is computationally less demanding and ensures good accuracy for fixed bodies (such as the passive grids here considered) as well as for bodies with prescribed motion (thus being potentially used for the simulation of active grids). Instead, when the dynamics is fully governed by the resulting fluid-structure interaction (e.g., the flapping flag), the second method, which is based on a moving-least-squares (MLS) interpolation, is more effective in minimising the spurious numerical oscillations<sup>49</sup>. Both methods have been extensively validated and used for multiphase and biological FSI problems<sup>9,44,47,48,50,51</sup>.

A two-dimensional spring-network structural model is used for simulating the deformable bodies<sup>44</sup>. The flag is modeled as a thin elastic membrane and discretised onto a Lagrangian mesh made of triangular elements. The mass is distributed on the vertices of the triangles which are connected by different types of springs to model both the in-plane and out-plane deformation<sup>52</sup>. In our case, we set the spring coefficients so that the flag is essentially inextensible and the only parameter controlling the elasticity is the bending stiffness  $B$ . Note that, as the Eulerian grid for the fluid flow is refined, the Lagrangian resolution has to be increased as well to ensure the correct enforcement of the no-slip boundary condition. To decouple this constraint (arising from the fluid-solid coupling) from the structural solver, an adaptive Lagrangian tiling procedure is performed, allowing to reduce the number of Lagrangian nodes used by the structural solver and to retain the same mesh independently of the Eulerian grid resolution<sup>47</sup>.

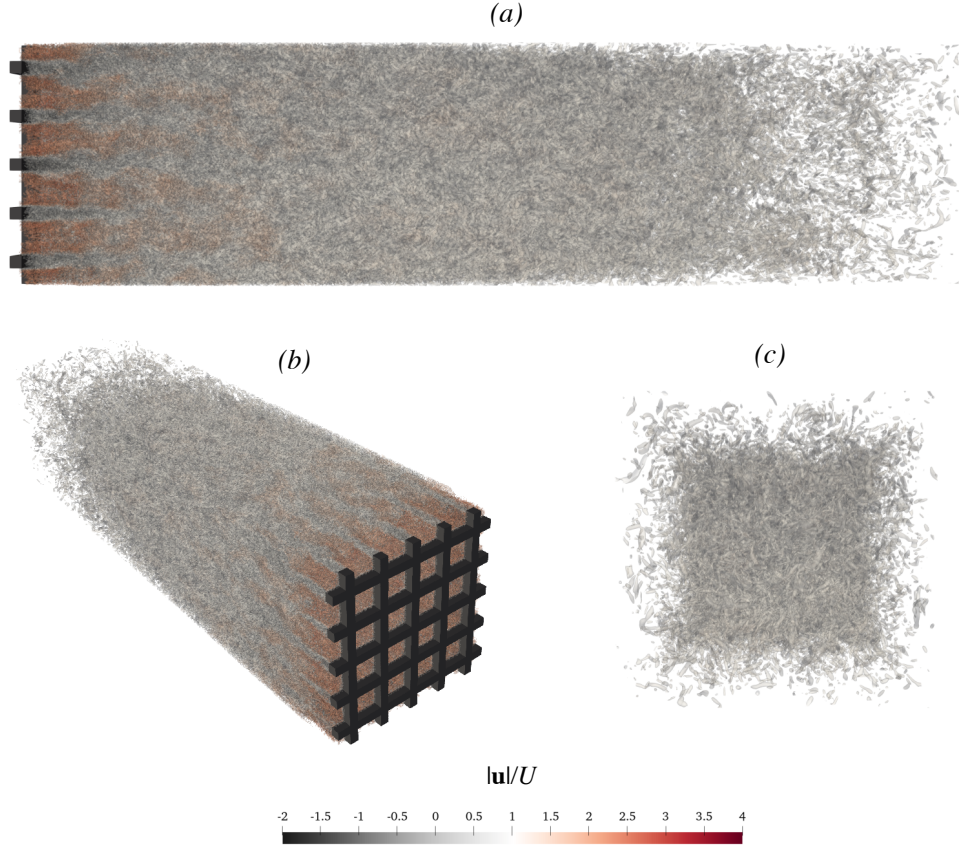


FIG. 3. Snapshots from DNS of grid-induced turbulence at  $Re_M = 5000$ : (a) sideview, (b) 3-D view and (c) backview. The figure shows the instantaneous vortical structures detected using the  $Q$ -criterion and coloured by the streamwise fluid velocity (from black to red).

A final note regards the code implementation and parallel computing performance. In this work, we employ the porting of the existing CPU version (using hybrid MPI/OpenMP parallelisation) to GPU-accelerated architectures using the CUDA Fortran library and an extensive use of CUF kernel directives<sup>45,53</sup>. A (one-dimensional) slab domain decomposition is used to distribute the simulation over four NVIDIA Tesla V100 GPUs using the Saion cluster at OIST. In the baseline configurations explained in the following sections, the computing time per iteration is about 0.075 s for the characterisation of grid-induced turbulence (Sec. III) and 0.13 s for the complete simulation of the FSI problem (Sec. IV).

### III. CHARACTERISATION OF GRID-INDUCED TURBULENCE

As a first step, we focus on characterising the turbulent flow that is generated by the presence of the fixed grid. To this aim, we maximise the streamwise domain extension to  $L_x = 120M$ , whereas for the transverse (vertical and spanwise) directions a much smaller extension of  $L_y = L_z = 5M$  is used. The simulations are carried out on a uniform Eulerian mesh made of  $3072 \times 128 \times 128$  nodes using a fixed timestep  $\Delta t U/M = 5 \times 10^{-4}$ . Results on the convergence with respect to the mesh resolution and transverse domain extension are reported in Appendix A, showing only a minimal influence on the main quantities of interest.

The study is performed considering two different Reynolds numbers: (i)  $\text{Re}_M = 1000$  that will be the configuration used for the complete FSI simulation (see next Section IV) and (ii)  $\text{Re}_M = 5000$  that will be considered here for a more detailed analysis and to perform a comparison with the experimental data of Ref.<sup>31</sup>. The simulations are advanced in time up to  $tU/M = 4000$  in order to achieve statistical convergence. We disregard the initial transient and start accumulating the statistics once the turbulence is fully developed throughout the domain. The quantities of interest are computed by sampling the flow time history with a stencil of  $2151 \times 3 \times 3$  virtual probes arranged around the centerline (with a uniform spacing of  $M/2$  in the streamwise direction and  $2M/3$  in the transverse directions) and making use of Taylor’s frozen turbulence hypothesis. Additionally, at  $\text{Re}_M = 5000$  we extract a number of slices in the transverse homogeneous plane (which are evenly-spaced in the streamwise direction by  $5M$ ) for computing the energy spectra along with the same aforementioned quantities.

Fig. 3 provides a snapshot from the simulation at  $\text{Re}_M = 5000$ . For a better visualisation close to the grid, only the region up to  $x/M \approx 25$  in the streamwise extent is shown instead of the full extent of the domain  $x/M \approx 120$ . From both the side and 3-D views in Fig. 3(a,b), qualitative insight is given on how turbulence is first generated in the vicinity of the grid and then starts to decay as the streamwise distance further increases. Moreover, it can be observed that the characteristic size of the vortical structures, here detected as the isosurfaces of the positive second invariant of the velocity gradient  $Q^{54}$ , increases with the distance from the grid. On the other hand, the flow appears to be statistically homogeneous along the  $y$  and  $z$  direction, Fig. 3(c), as expected. Consequently, when referring to the transverse component we will consider the average between these two directions.

Fig. 4 shows the main quantities characterising the turbulent flow as a function of the normal-

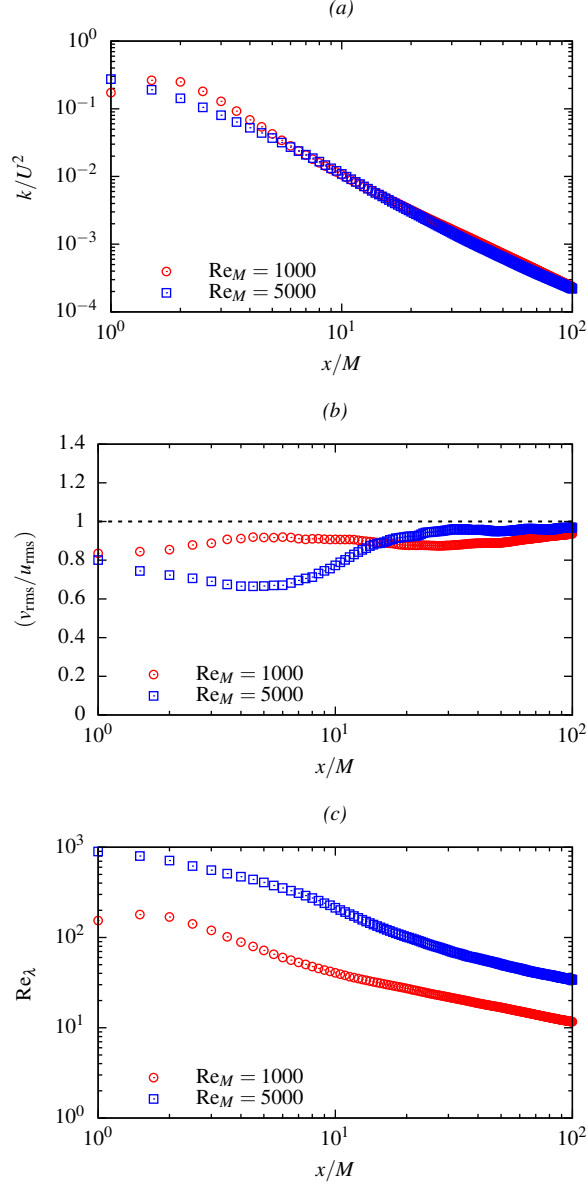


FIG. 4. Grid-induced turbulence main quantities as a function of the normalized streamwise coordinate: (a) turbulent kinetic energy; (b) large-scale anisotropy; (c) Reynolds number based on the Taylor lengthscale. Two different Reynolds numbers are tested:  $Re = 1000$  (red circles) and  $5000$  (blue squares).

ized streamwise coordinate  $x/M$ : (a) the (normalized) turbulent kinetic energy, (b) the large-scale flow anisotropy and (c) the micro-scale (or turbulent) Reynolds number. The turbulent kinetic energy  $k/U^2$  (where  $k = \langle u^2 + v^2 + w^2 \rangle / 2$ ) is shown in Fig. 4(a). The characteristic scenario of decaying turbulence can be noticed, so that the range of observation can be roughly divided in two regions: a *production* region (for  $x/M \lesssim 10$ ) where turbulence is developed and a *decay* region (for

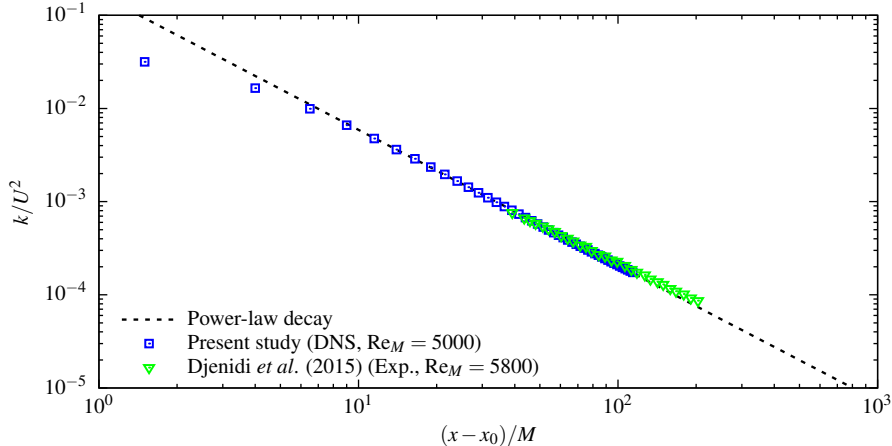


FIG. 5. Comparison of DNS results of turbulent kinetic energy at  $Re_M = 5000$  with the experimental measurements of Djenidi, Kamruzzaman, and Antonia<sup>31</sup> and power-law fitting, Eq. (4). Note that the quantities are plotted as a function of the adjusted streamwise distance using the virtual origin  $x_0$ .

$x/M \gtrsim 10$ ) where the turbulent kinetic energy approximately follows the well known power-law decay (1). Note that, although the differences observed for increasing  $Re_M$  appear rather minimal, they may reflect, in particular, in a certain variation of the decay exponent  $n$ <sup>31</sup>. Next, we look at the (large-scale) anisotropy of the flow by considering the ratio between the streamwise and transverse velocity fluctuations  $v_{rms}/u_{rms}$ , reported in Fig. 4(b). Approaching the decay region (i.e., for  $x/M \gtrsim 10$ ), this quantity appears to be approximately constant in a large portion of the observed range, with  $v_{rms}/u_{rms}$  varying between about 0.8 and 1. A more evident influence of the Reynolds number can be noticed with the flow becoming more isotropic when increasing  $Re_M$ , as expected. At  $Re_M = 5000$ , in particular, an essentially isotropic region is observed for  $x/M \gtrsim 30$ . Finally, the micro-scale Reynolds number  $Re_\lambda = \lambda_f u_{rms}/\nu$ , based on the (longitudinal) Taylor lengthscale  $\lambda_f$ , is shown in Fig. 4(c). Overall,  $Re_\lambda$  is decreasing with the streamwise coordinate although with a relatively slow decay rate. As expected, a remarkable variation of this quantity is observed when varying  $Re_M$ . On the other hand, the difficulty in achieving a large micro-scale Reynolds number, i.e.  $Re_\lambda \gtrsim 10^2$ , using a classical passive grid is well known<sup>55</sup>.

Our results obtained at  $Re_M = 5000$  can be representative of typical grid-induced turbulence conditions and are therefore compared in Fig. 5 with the experimental measurements reported by Djenidi, Kamruzzaman, and Antonia<sup>31</sup>. Specifically, we compare with their findings at  $Re_M = 5800$  using a perforated grid with square holes having solidity  $\sigma \approx 43\%$  (indicated as SSQ43 in Ref.<sup>31</sup>). Despite the minor discrepancies due to non-negligible difference in the nominal pa-

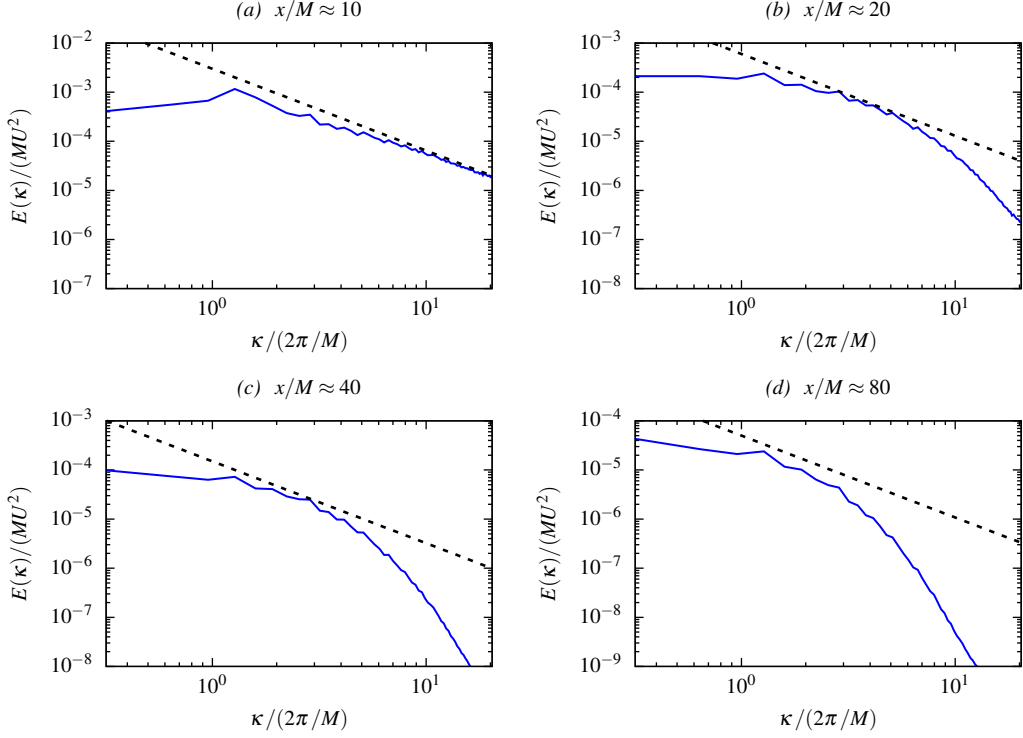


FIG. 6. Energy spectra of turbulent flow at  $\text{Re}_M = 5000$  at four different streamwise locations from the grid: (a)  $x/M \approx 10$ , (b)  $x/M \approx 20$ , (c)  $x/M \approx 40$ , (d)  $x/M \approx 80$ . The dashed line indicates the characteristic Kolmogorov scaling  $\kappa^{-5/3}$  in the inertial subrange.

rameters, the numerical data appear to be fully consistent with similar experimental evidence. Furthermore, as shown in Fig. 5, we quantitatively assess the decay of the turbulent kinetic energy by fitting our data to the well-known power-law expression<sup>27</sup>

$$\frac{k}{U^2} = A \frac{(x - x_0)^{-n}}{M}, \quad (4)$$

where three free parameters appear: a multiplicative factor  $A$ , the virtual origin  $x_0$  and the decay exponent  $n > 0$ . The delicate issue of how to perform accurately the fitting procedure has been discussed by several authors, see e.g. Refs.<sup>27,29,30</sup>. Moreover, Ref.<sup>31</sup> recently revised the applicability of Eq. (4), suggesting the use of a modified form where the decay exponent is not constant. Here, we adopt the classical form and perform the fitting procedure as follows: firstly, we deduce the most appropriate value for the virtual origin  $x_0$  on a trial-and-error basis by varying this parameter in order to observe the most extended range of power-law decay when plotting  $k$ , or equivalently the most horizontal plateau when plotting  $\lambda^2/[M(x - x_0)]$ , as a function of  $(x - x_0)$ <sup>29</sup>. Then, while keeping fixed the virtual origin, we perform a least-squares fit to obtain the other two param-

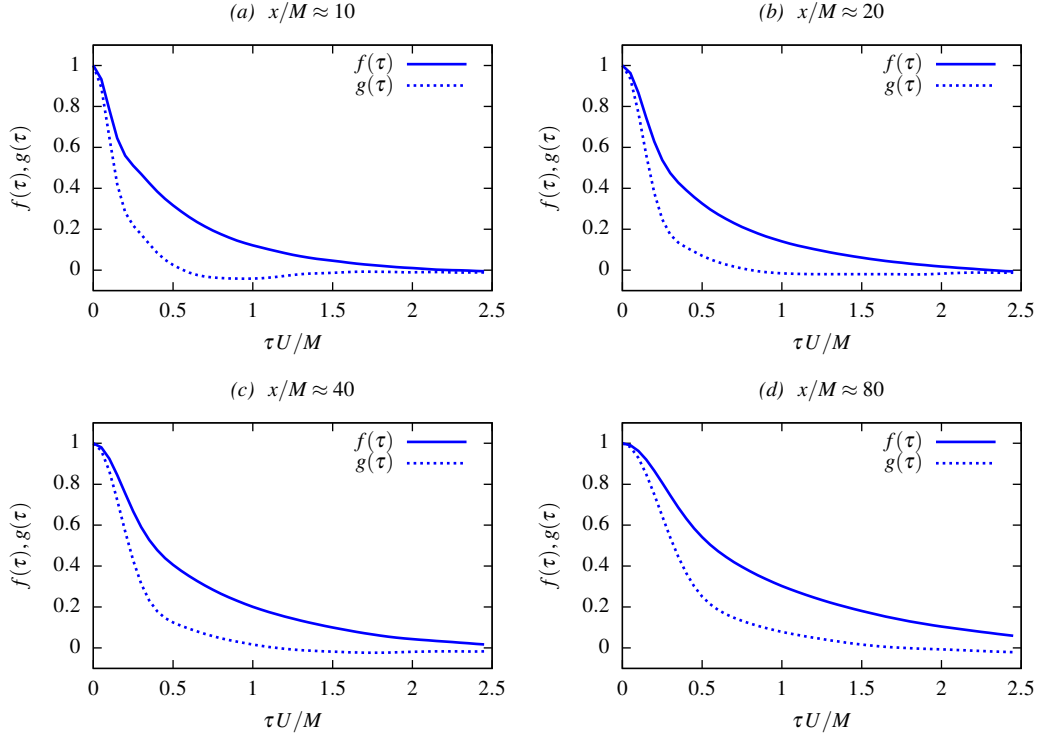


FIG. 7. Velocity autocorrelation coefficients of turbulent flow at  $\text{Re}_M = 5000$  at four different streamwise locations from the grid: (a)  $x/M \approx 10$ , (b)  $x/M \approx 20$ , (c)  $x/M \approx 40$ , (d)  $x/M \approx 80$ . The longitudinal and transverse autocorrelation coefficients, defined by Eqs. (5) and (6), are denoted by  $f(\tau)$  and  $g(\tau)$ , respectively.

ters,  $A$  and  $n$ . The following values are obtained and used for plotting the power-law in Fig. 5(a):  $A = 0.17$ ,  $x_0/M = 4$  and  $n = 1.45$ . Despite the well-known sensitivity of  $n$  with respect to the flow properties as well as the details of the measurement method, our data are in good agreement with DNS results reported in the literature<sup>31</sup>. Lastly, we point out that the slight deviation of the experimental measures shown in Fig. 5 is consistent with the different nominal Reynolds number.

Fig. 6 shows the turbulent energy spectra  $E(\kappa)$  computed at four streamwise locations  $x/M \approx \{10, 20, 40, 80\}$ . It can be observed that  $x/M \approx 10$  corresponds to the very early onset of the decay region. The numerical results are compared with the classical Kolmogorov scaling  $k^{-5/3}$  that is expected for the inertial subrange. Taking into account the moderate Reynolds number achieved in our configuration, it can be noticed a reasonable agreement with such prediction. Comparing the different panels, it can be appreciated how the turbulent kinetic energy (i.e., the integral of the spectrum) progressively decays for increasing  $x/M$ . In fact, using the corresponding values of the

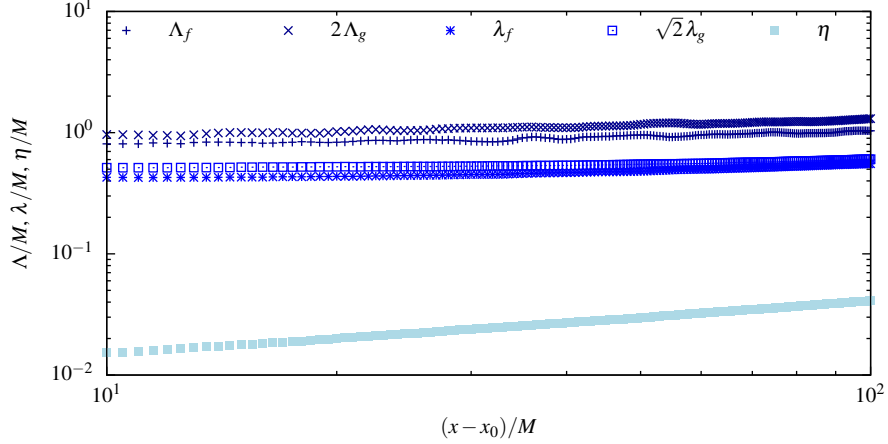


FIG. 8. Overview of characteristic, i.e., integral (dark blue), Taylor (blue) and Kolmogorov (light blue), lengthscales at  $\text{Re}_M = 5000$ . The transverse (integral and Taylor) lengthscales are multiplied to match the longitudinal ones by the corresponding factors predicted in the case of isotropic turbulence.

integral lengthscale and turbulent kinetic energy, it is possible to normalise these plots with all curves collapsing on each other within the inertial subrange (not shown).

Fig. 7 collects the plots of the velocity autocorrelation coefficients at the same four streamwise locations  $x/M \approx \{10, 20, 40, 80\}$ . We define the longitudinal and transverse autocorrelation coefficients,  $f(\tau)$  and  $g(\tau)$ , respectively as:

$$f(\tau) = \frac{\langle u(\mathbf{x} + \tau U \mathbf{e}_x) u(\mathbf{x}) \rangle}{\langle u^2(\mathbf{x}) \rangle}, \quad (5)$$

$$g(\tau) = \frac{\langle v(\mathbf{x} + \tau U \mathbf{e}_x) v(\mathbf{x}) \rangle}{\langle v^2(\mathbf{x}) \rangle}, \quad (6)$$

where  $\tau$  is the temporal separation. Taylor's frozen turbulence hypothesis is used to relate the temporal and spatial separation, i.e. we assume  $r_x \approx \tau U$ . The validity of such assumption has been directly verified by evaluating the equality  $\partial_t u + U \partial_x u \approx 0$  throughout the fluid domain. The autocorrelation coefficients are used to compute the characteristic lengthscales of the turbulent flow. Looking at Fig. 7, the autocorrelation is essentially going to zero for  $\tau U/M \approx 2.5$ , thus confirming that the transverse domain extension is sufficient to describe the whole range of scales of fluid motion.

An overview of how the characteristic lengthscales of the turbulent flow (i.e. integral, Taylor and Kolmogorov scales) evolve approximately within the decay region is given in Fig. 8. Such lengthscales are obtained from the autocorrelation coefficients and properly defined in the following. Firstly, the integral lengthscales  $\Lambda$  are representative of the largest turbulent eddies and

are computed by integrating the corresponding autocorrelation coefficient over the range of separation. In Fig. 8, the transverse scale is multiplied by 2 in order to graphically corroborate the prediction  $\Lambda_f = 2\Lambda_g$  obtained for isotropic turbulence<sup>56</sup> (where  $\Lambda_f$  and  $\Lambda_g$  are the longitudinal and transverse integral lengthscales, respectively). It is also evident that  $\Lambda_f \approx 2\Lambda_g \approx M$ , i.e. the integral lengthscale is substantially comparable with the grid spacing, although it progressively increases with  $x/M$ . Nevertheless, this further confirms that the chosen domain is adequate to correctly capture the largest existing flow structures. Next, the Taylor lengthscales  $\lambda$  representative of intermediate-size eddies are obtained after a Taylor series expansion of the corresponding autocorrelation coefficient near the origin<sup>56</sup>. The theoretical background for isotropic turbulence yields  $\lambda_f/\lambda_g = \sqrt{2}$ . In Fig. 8 we account for this factor to relate the longitudinal and transverse scales, showing very good agreement especially when approaching the region where the flow becomes more isotropic (see Fig. 4(b)). Lastly, we focus on the smallest flow scales dominated by viscous dissipation. We compute the energy dissipation rate as  $\varepsilon = 30\nu u_{\text{rms}}^2/\lambda_f^2 = 15\nu u_{\text{rms}}^2/\lambda_g^2$  and obtain the Kolmogorov lengthscale  $\eta = (\nu^3/\varepsilon)^{1/4}$ <sup>57</sup>. The evolution of the latter is depicted in Fig. 8, showing a tendency to grow with the streamwise coordinate as the turbulent eddies decay and diffuse similar to the other characteristic scales (although according to different scaling laws<sup>30</sup>).

#### IV. FLAPPING FLAG IN GRID TURBULENCE

In this Section, the flag-in-the-wind FSI problem is investigated in the case of a turbulent incoming flow. The setup is depicted in Fig. 1 where the grid-induced turbulence is investing the flag and perturbing the flapping motion that would naturally arise in the laminar case.

To control the turbulent intensity  $Tu = \sqrt{\frac{2}{3}k}/U$  in the proximity of the flag, we vary the distance from the grid  $X_{\text{LE}}/M$  at which the leading edge (LE) is placed. Two distances  $X_{\text{LE}}/M = \{4, 8\}$  that correspond to  $Tu \approx \{40\%, 20\%\}$  are tested. Additionally, the simulation at  $Tu = 0$  (i.e.,  $X_{\text{LE}}/M \rightarrow \infty$ ) is performed by removing the grid. After validating our numerical method (see Appendix A), the analysis is performed at  $\text{Re}_L = 1000$  to achieve a configuration where the incoming flow shows the essential features of grid turbulence, as shown in Sec. III. The simulations are carried out on a uniform mesh made of  $900 \times 300 \times 300$  nodes using a fixed timestep  $\Delta t U/M = 5 \times 10^{-4}$ , reaching a final time of  $tU/M = 300$ . Specifically, the domain extension is set to  $L_x = 12M$  and  $L_y = L_z = 4M$  whereas the grid resolution is improved in order to better describe the flow details close to the flag and consequently the coupled flapping dynamics. Note that our focus is on strong

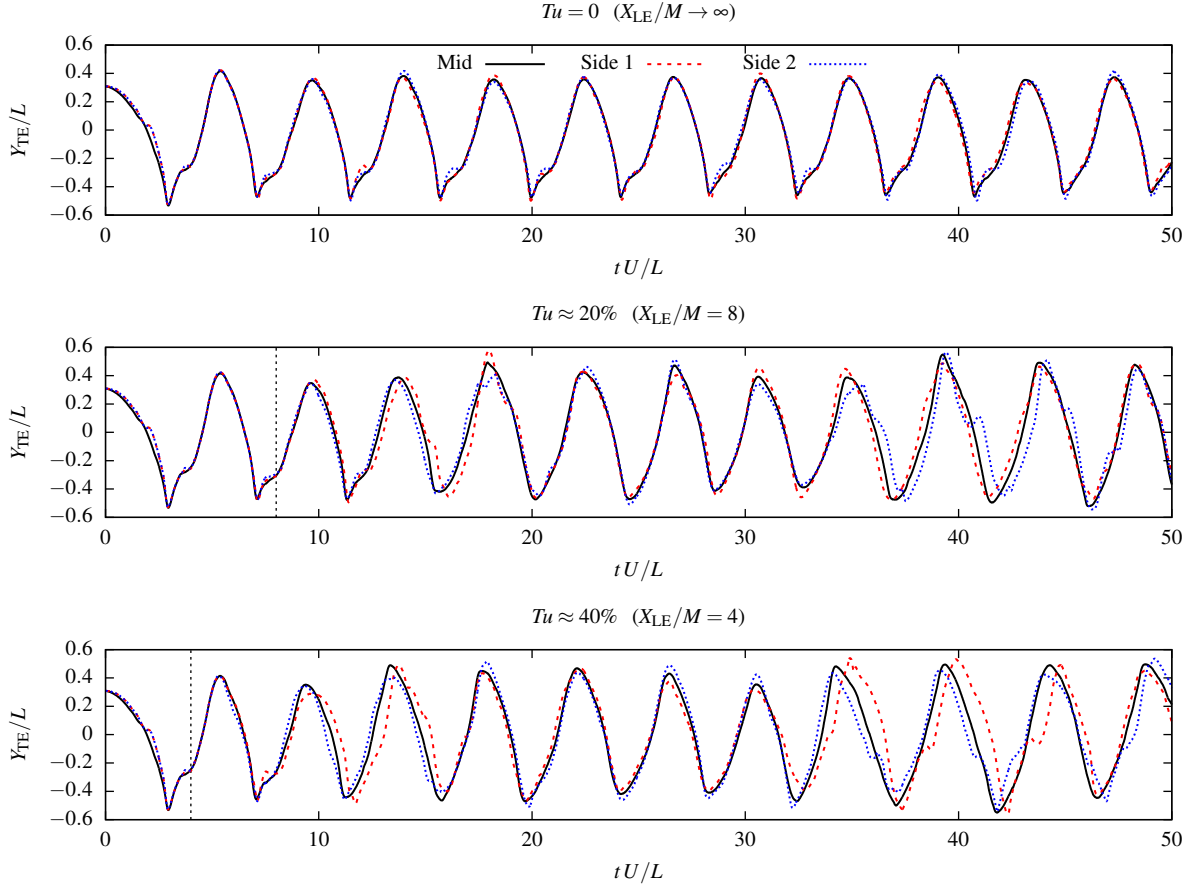


FIG. 9. Time history of trailing edge middle (solid black) and side (dashed red and dotted blue) points of flapping flag at different turbulence intensities. The plots show the initial stage of the simulation. For  $Tu \approx \{20\%, 40\%\}$  the vertical dashed line indicates the time  $X_{LE}/U$  at which the turbulent front reaches the flag.

turbulent fluctuations that are achieved by placing the flag at a relatively short distance from the grid, but sufficiently far from the highly inhomogeneous region immediately downstream of the grid.

Fig. 9 collects the time history of the trailing edge (TE) transverse motion for each of the investigated configurations. It is worth noticing a close resemblance of the results in the early stage of the simulation (i.e., approximately within the first flapping cycle). As graphically shown in the corresponding plots, this is simply explained by the fact that for  $Tu \approx \{20\%, 40\%\}$  the turbulent front has not reached the flag yet. The flapping motion is therefore always triggered in the same way as the laminar case. However, after few flapping cycles a deviation of the turbulent cases from the latter becomes evident, i.e., when the perturbation exerted by the incoming grid

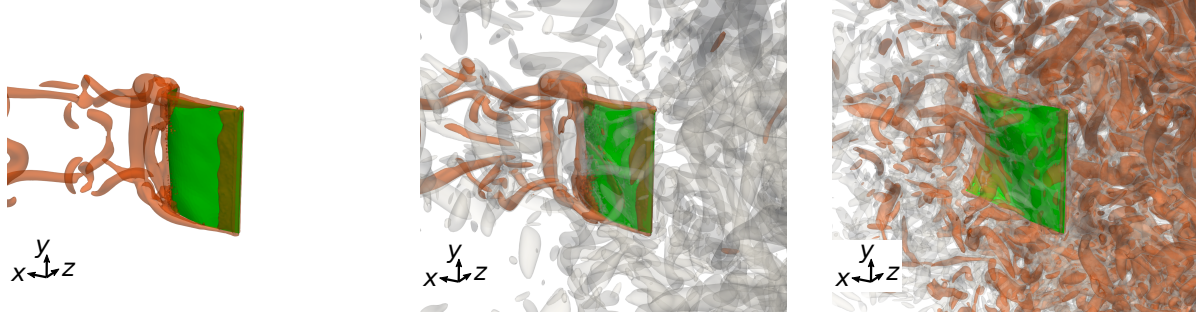


FIG. 10. Instantaneous vortical structures in proximity of the flapping flag at different turbulence intensities (left:  $Tu = 0$ ; centre:  $Tu = 20\%$ ; right:  $Tu = 40\%$ ). Isosurfaces detected using  $Q$ -criterion of lower (white) and higher (orange) intensity are denoted by different colour.

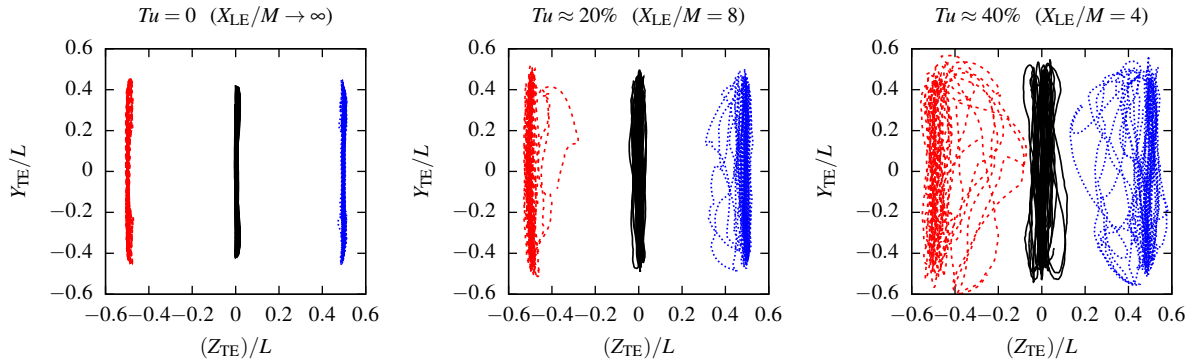


FIG. 11. Front-view trajectories of trailing edge middle (black) and side (red and blue) points at different turbulence intensities in the statistically steady state.

turbulence is effective. As a result, the oscillation becomes less regular with a clear variation of the peak-to-peak amplitude for increasing  $Tu$ . On the other hand, it has to be pointed out that the aeroelastic instability appears to be robust, thus remaining the main mechanism driving the self-sustained motion of the flag. For a deeper understanding, Fig. 9 shows the time history for both the TE side and mid points. In the laminar case, the differences between these observables are negligible, thus suggesting that the motion is essentially two-dimensional with no significant activation modes in the spanwise direction. Conversely, this is not the case in the presence of incoming turbulence, as indicated by the shift between the side and mid point time traces. Such effect is clearly more pronounced when increasing the turbulence intensity.

To gain qualitative insight, Fig. 10 provides a visual comparison between the three cases focusing on the vortical flow structures detected using  $Q$ -criterion. In the laminar case ( $Tu = 0$ ),

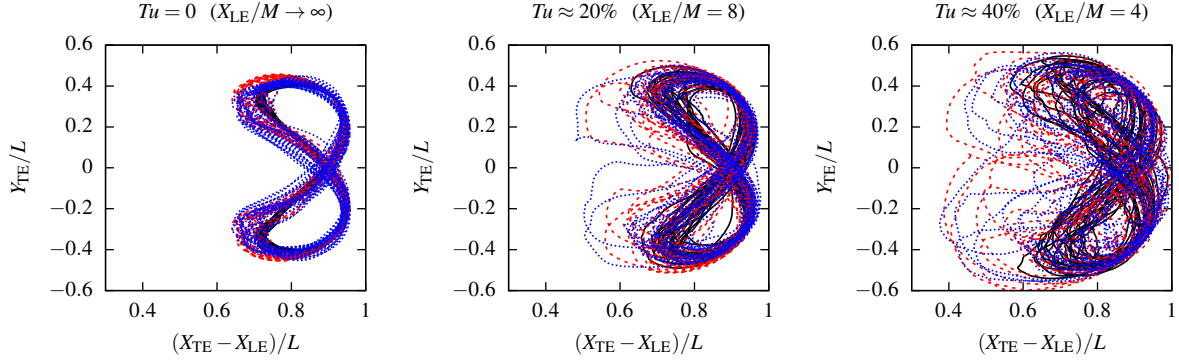


FIG. 12. Side-view trajectories of trailing edge middle (black) and side (red and blue) points at different turbulence intensities in the statistically steady state.

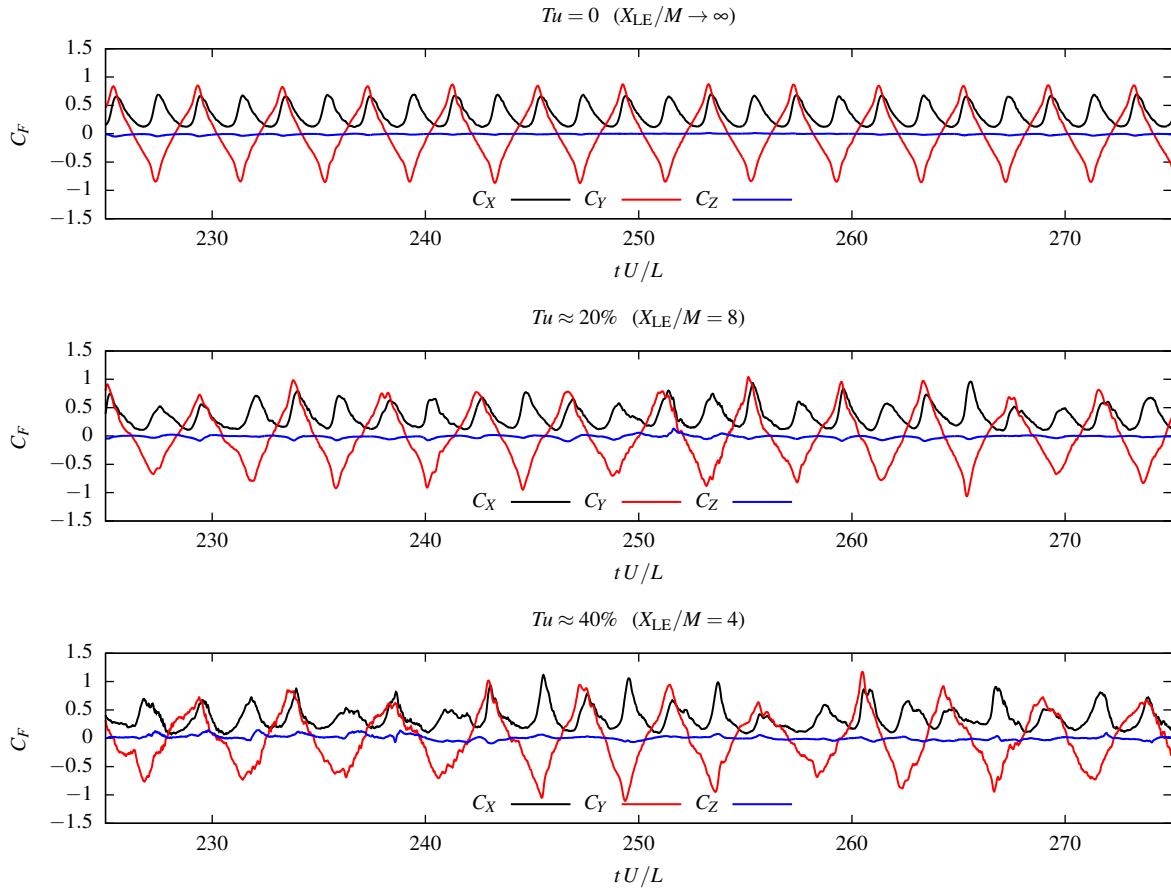


FIG. 13. Time history of side (black), lift (blue) and drag (red) force coefficients at different turbulence intensities in the statistically steady state.

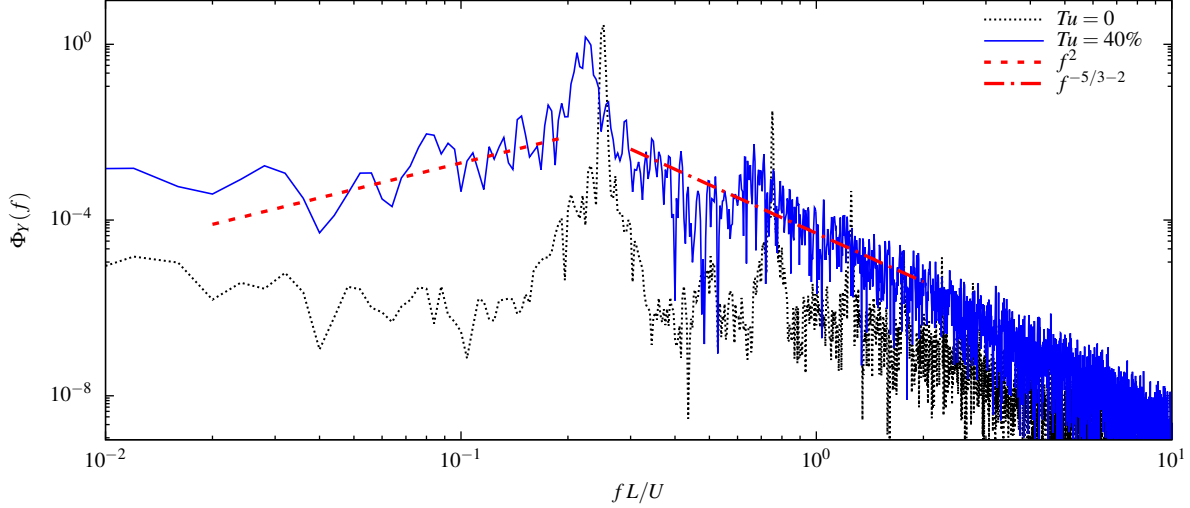


FIG. 14. Power spectral density of TE (mid point) transverse motion for the laminar ( $Tu = 0$ ) and the turbulent case at  $Tu = 40\%$ . The latter is compared with the scaling laws proposed by Jin, Ji, and Chamorro<sup>15</sup>.

the characteristic wake pattern of the self-sustained flapping is obtained. In the intermediate case ( $Tu = 20\%$ ), such signature is still found, whereas it is eventually lost for the highest turbulence level ( $Tu = 40\%$ ). In the latter case, the flag deformation is more three-dimensional with a visible bending along the spanwise direction that is not present in the laminar case.

The observation can be complemented by looking at the trajectories of the three points (i.e., middle and side points) from both the front and side view, shown in Fig. 11 and Fig. 12, respectively (we restrict now our attention to the statistically steady regime). An overall trend toward a more chaotic and three-dimensional motion is clearly observed. In particular, the characteristic shape of the limit-cycle oscillation (LCO) of the flapping flag in uniform flow is progressively lost as the turbulence level is increased. The same outcome can be obtained from the time histories of the aerodynamic coefficients reported in Fig. 13. Consistently with what observed for the TE motion, both the lift, side and drag coefficients become more irregular as the turbulence intensity increases.

The effect of turbulence is reflected in the spectral content of the oscillation time history, shown in Fig. 14, where a much more broadband distribution can be observed for  $Tu = 40\%$  when compared to the laminar case ( $Tu = 0$ ). Furthermore, the dominant peak associated with the flapping frequency  $f_{\text{flap}}$ , which can be expressed in nondimensional terms by the Strouhal number  $St = f_{\text{flap}}L/U$ , is also smoothed and found to decrease. To characterise the modification observed in the spectrum, we apply to our problem the dynamical model recently proposed by Jin, Ji, and

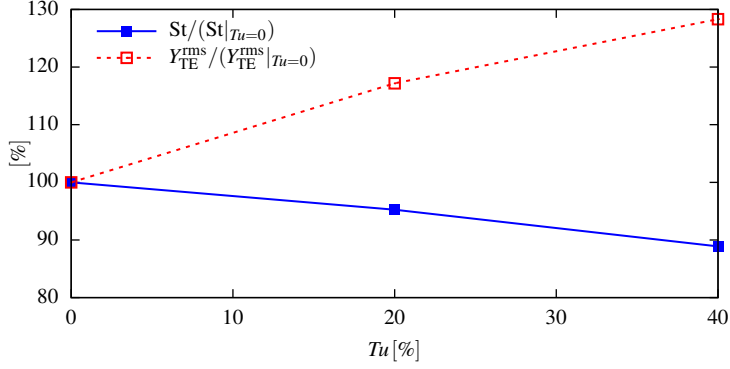


FIG. 15. Variation of Strouhal number and r.m.s. of TE (mid point) transverse oscillation with respect to the laminar case ( $Tu = 0$ ) as a function of the turbulence intensity.

Chamorro<sup>15</sup> for oscillating plates in active grid turbulence. By combining a forced-oscillator model and phenomenological arguments based on Kolmogorov theory, the following scalings for the oscillation spectrum can be argued<sup>15</sup>: (i)  $\Phi_Y \propto f^2$  in the low-frequency region (i.e., for  $f$  smaller than the natural frequency in the case of oscillating plate and such that the turbulence spectrum is approximately constant); (ii)  $\Phi_Y \propto f^{-5/3-2}$  for the intermediate-frequency region (i.e., for  $f$  larger than the natural frequency and such that the turbulence spectrum is within the inertial subrange). We underline that in our case the dominant frequency is determined by the nonlinear mutual interaction between the fluid and structural response. Moreover, the underlying assumptions of the model are not strictly met due to the limited Reynolds number (i.e., no clear inertial range can be observed) and distance from the grid (i.e., the flag is not properly within the decay region). Notwithstanding, in Fig. 14 a reasonable agreement can be noticed between the theoretical prediction and the numerical results for the turbulent case, while similar power-law subranges are not observed for the laminar case. As expected in light of the aforementioned flow conditions, the major discrepancy is found in the intermediate-frequency region, whereas in the low-frequency region the numerical evidence agree well with the model prediction. This findings thus suggests that the fingerprint of turbulent fluctuations clearly appears in the resulting structural response.

To conclude the analysis, we look at how the Strouhal number and the flapping amplitude, i.e., the main quantities characterising the flapping motion, systematically vary with  $Tu$ . The relative change of these two observables is reported in Fig. 15, where both quantities are normalised with the reference value obtained in the laminar case. As already noted, the Strouhal number decreases

with the turbulence intensity. Conversely, the amplitude of the transverse motion, characterised in the chaotic case by the root-mean-square  $Y_{TE}^{rms}$ , is found to increase with  $Tu$ . A monotonic trend is observed for both  $St$  and  $Y_{TE}^{rms}$ , with the maximum variation of about  $-10\%$  and  $+30\%$  at the highest  $Tu = 40\%$ , indicating that the effect of turbulence can also be relevant from a quantitative viewpoint.

## V. SUMMARY AND PERSPECTIVES

In order to advance the current knowledge on fluid-structure interaction (mainly limited to the case of laminar flows), this work concerned the revisited study of the three-dimensional flag-in-the-wind problem in the framework of grid-induced turbulence. Grid turbulence is relevant from both the fundamental and applied viewpoint, but few numerical studies can be found in this regard due to the highly-demanding computational requirements imposed by the problem, in particular when considering the FSI simulation. To this aim, we performed fully-resolved direct numerical simulations exploiting state-of-the-art immersed boundary methods to properly describe the way in which turbulence is generated in the vicinity of the grid, as well as the coupled FSI dynamics of the flapping flag in both laminar and turbulent flow. The problem is tackled by taking advantage of the great potential of GPU-accelerated parallel computing and the computational framework here proposed is validated with respect to related experimental and numerical literature.

Specifically, we investigated the dynamics of a conventional flag (i.e., hinged at its leading edge) when immersed in the turbulence generated by regular passive grids at moderate Reynolds numbers. First, the turbulent flow was characterised in details, including the evaluation of the power-law decay and the comparison with experimental measurements in similar conditions. Furthermore, the energy distribution is shown by means of a scale-by-scale analysis. Then, we analysed the influence of the turbulent intensity on the flapping flag dynamics. We found that, although the overall trend towards a more chaotic motion is clearly noticed, the aeroelastic instability, and consequently the self-sustained flapping mechanism, still manifests also at the strongest turbulence level here considered. However, the effect of fluctuations impacting the body is such that the main features of the oscillations (including their amplitude and frequency) are remarkably affected. In particular, the flapping frequency (i.e., Strouhal number) is found to decrease whereas the amplitude increases with the turbulence intensity. Moreover, in agreement with recent experimental investigations<sup>15</sup>, the fingerprint of turbulence can be detected and qualitatively described

by looking at the spectral content of the altered oscillation.

In conclusion, our findings are relevant from a fundamental perspective, suggesting a general description for the enriched dynamical scenario of FSI in turbulence, as well as for several applications, such as flow control and energy harvesting in a more general configuration typical of real-world fluid flows.

## ACKNOWLEDGMENTS

The authors acknowledge fruitful discussions with Prof. Roberto Verzicco (University of Roma ‘Tor Vergata’). S.O. and M.E.R. acknowledge the computer time provided by the Scientific Computing section of Research Support Division at OIST. A.M. thanks the financial support from the Compagnia di San Paolo, project MINIERA n. I34I20000380007.

## Appendix A: Validation and convergence study

### 1. Grid-induced turbulence

Concerning the numerical characterisation of grid-induced turbulence (Sec. III), the sensitivity of our results has been checked with respect to both spatial and temporal resolution, as well as to the transverse domain extension. Here, we focus on the former and the latter, since the influence of decreasing the simulation timestep was found to be negligible (not shown). A convergence analysis has been performed considering the case  $Re_M = 5000$ . For the spatial resolution, we have performed a simulation where the mesh spacing  $\Delta x$  is halved, i.e., doubling the resolution of the baseline configuration. For the transverse domain extension, we doubled both  $L_y$  and  $L_z$  while maintaining the same mesh spacing. To retain a feasible computational time while increasing the number of mesh points, we have decreased the streamwise domain extension to  $L_x/M = 40$  and  $60$ , respectively. In order to have a faster statistical convergence, we take advantage of the increased number of points and perform a spatial average for the quantities of interest over the transverse slices.

Figure 16 shows the results from these tests compared with those obtained using the baseline configuration adopted in the present work, in terms of the same quantities presented in Sec. III, i.e., turbulent kinetic energy (Fig. 16(a)), large-scale anisotropy (Fig. 16(b)) and turbulent Reynolds number (Fig. 16(c)). It can be noticed that the numerical results are overall robust. In particular,

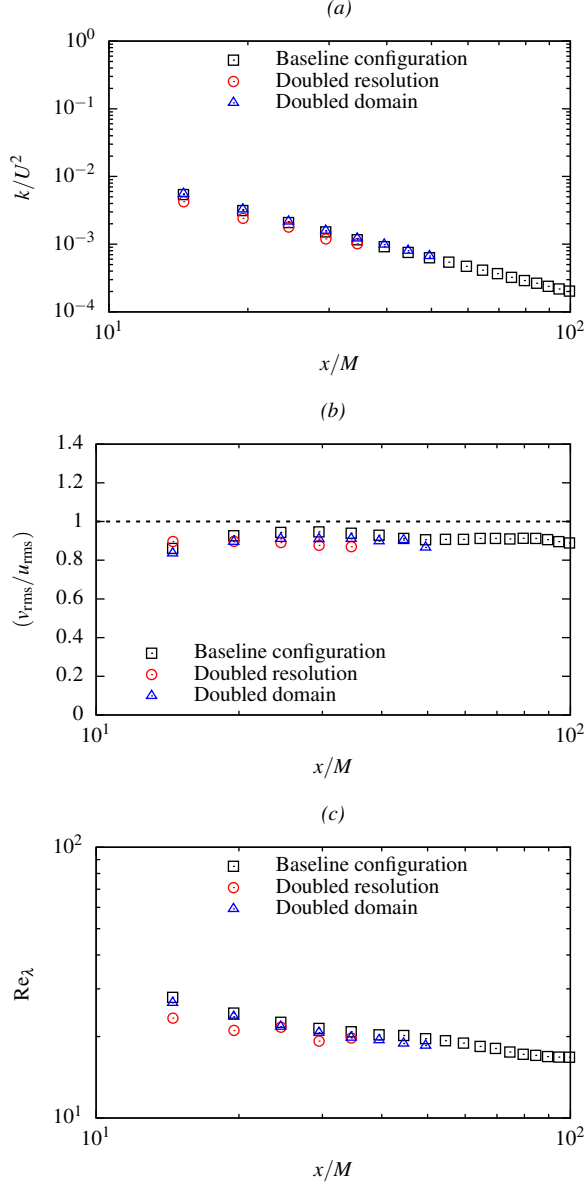


FIG. 16. Convergence study on grid turbulence properties at  $Re_M = 5000$  with respect to mesh resolution (red circles) and transverse domain extension (blue triangles) versus the baseline configuration adopted in the present work (black squares): (a) turbulent kinetic energy; (b) ratio between transverse and streamwise turbulent fluctuations; (c) Reynolds number based on Taylor lengthscale. All quantities are reported as a function of the normalized streamwise coordinate.

the influence of the domain extension appears to be minimal. On the other hand, the variation observed when refining the mesh resolution is more evident, although still small. Indeed, the latter can be linked to the aforementioned dependency of the generated turbulence on the small-

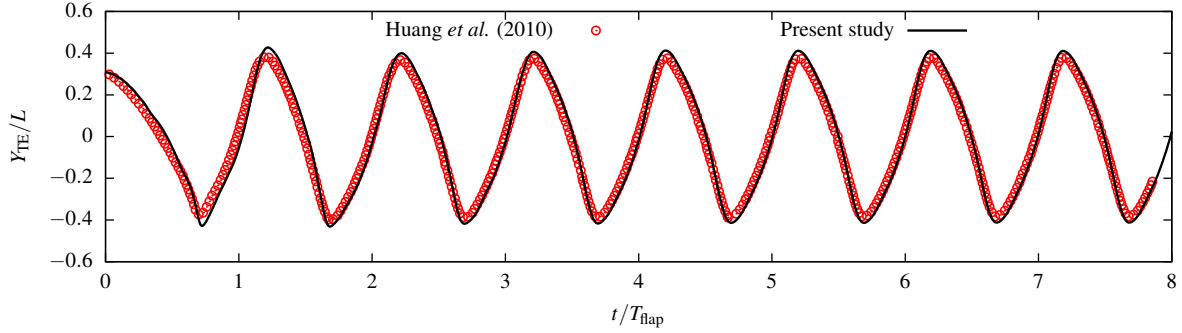


FIG. 17. Time history of the trailing edge mid point for flapping flag in laminar flow at  $Re_L = 200$ . Comparison between the present results (black line) and those by Huang and Sung<sup>40</sup> (red symbols).

scale details associated with boundary-layer effects and flow separation in the proximity of the grid. Nevertheless, we remark that our findings obtained with the baseline configuration are in good agreement with experimental measurements using a similar setting (see Fig. 5), therefore confirming that the chosen resolution is adequate to describe the essential features of the turbulent flow in the region of interest.

## 2. Flapping flag in laminar flow

To check the accuracy of the FSI simulation, we validate our numerical technique by considering the coupled motion of the flapping flag in a uniform flow at  $Re = 200$ . This configuration has been originally investigated by Huang and Sung<sup>40</sup> and later also by Refs.<sup>42–44</sup>. Focusing on the time history of the transverse oscillation (we consider only the TE mid point since the motion is essentially two-dimensional), Fig. 17 shows a comparison between our results and those by Huang and Sung<sup>40</sup>. Here, time is normalised using the corresponding flapping period (differing only about 2%). A good agreement can be observed both in the shape and amplitude of the oscillation indicating that the numerical procedure is accurately reproducing the reference solution.

## DATA AVAILABILITY

The data that support the findings of this study are available from the corresponding author upon reasonable request.

## REFERENCES

- <sup>1</sup>T. Leclercq and E. de Langre, “Reconfiguration of elastic blades in oscillatory flow,” *Journal of Fluid Mechanics* , 606 (2018).
- <sup>2</sup>E. Loiseau, S. Gsell, A. Nommick, C. Jomard, D. Gras, P. Chanez, U. D’ortona, L. Kodjabachian, J. Favier, and A. Viallat, “Active mucus–cilia hydrodynamic coupling drives self-organization of human bronchial epithelium,” *Nature Physics* **16**, 1158–1164 (2020).
- <sup>3</sup>S. Tschisgale, B. Löhner, R. Meller, and J. Fröhlich, “Large eddy simulation of the fluid–structure interaction in an abstracted aquatic canopy consisting of flexible blades,” *Journal of Fluid Mechanics* **916** (2021).
- <sup>4</sup>J. Hobeck and D. Inman, “Artificial piezoelectric grass for energy harvesting from turbulence-induced vibration,” *Smart Materials and Structures* **21**, 105024 (2012).
- <sup>5</sup>S. Orrego, K. Shoele, A. Ruas, K. Doran, B. Caggiano, R. Mittal, and S. H. Kang, “Harvesting ambient wind energy with an inverted piezoelectric flag,” *Applied Energy* **194**, 212–222 (2017).
- <sup>6</sup>R. K. B. Gallegos and R. N. Sharma, “Flags as vortex generators for heat transfer enhancement: Gaps and challenges,” *Renewable and Sustainable Energy Reviews* **76**, 950–962 (2017).
- <sup>7</sup>G. Boccacero, S. Olivieri, A. Mazzino, and C. Boragno, “Power harvesting by electromagnetic coupling from wind-induced limit cycle oscillations,” *Smart Materials and Structures* **26**, 095031 (2017).
- <sup>8</sup>M. E. Rosti, M. Omidyeganeh, and A. Pinelli, “Passive control of the flow around unsteady aerofoils using a self-activated deployable flap,” *Journal of Turbulence* **19**, 204–228 (2018).
- <sup>9</sup>S. Olivieri, C. Boragno, R. Verzicco, and A. Mazzino, “Constructive interference in a network of elastically-bounded flapping plates,” *Journal of Fluids and Structures* **90**, 334–353 (2019).
- <sup>10</sup>J. M. McCarthy, S. Watkins, A. Deivasigamani, and S. J. John, “Fluttering energy harvesters in the wind: A review,” *Journal of Sound and Vibration* **361**, 355–377 (2016).
- <sup>11</sup>S. Olivieri, G. Boccacero, A. Mazzino, and C. Boragno, “Fluttering conditions of an energy harvester for autonomous powering,” *Renewable Energy* **105**, 530–538 (2017).
- <sup>12</sup>Y. Yu, Y. Liu, and X. Amandolese, “A review on fluid-induced flag vibrations,” *Applied Mechanics Reviews* **71** (2019).
- <sup>13</sup>R. M. C. So, X. Q. Wang, W.-C. Xie, and J. Zhu, “Free-stream turbulence effects on vortex-induced vibration and flow-induced force of an elastic cylinder,” *Journal of Fluids and Structures* **24**, 481–495 (2008).

- <sup>14</sup>J. Zhu, X. Wang, W.-C. Xie, and R. So, “Turbulence effects on fluidelastic instability of a cylinder in a shear flow,” *Journal of Sound and Vibration* **321**, 680–703 (2009).
- <sup>15</sup>Y. Jin, S. Ji, and L. P. Chamorro, “Spectral energy cascade of body rotations and oscillations under turbulence,” *Physical Review E* **94**, 063105 (2016).
- <sup>16</sup>W. K. George, “The decay of homogeneous isotropic turbulence,” *Physics of Fluids A: Fluid Dynamics* **4**, 1492–1509 (1992).
- <sup>17</sup>P.-Å. Krogstad and P. A. Davidson, “Is grid turbulence Saffman turbulence?” *Journal of Fluid Mechanics* **642**, 373 (2010).
- <sup>18</sup>P. A. Davidson, “The minimum energy decay rate in quasi-isotropic grid turbulence,” *Physics of Fluids* **23**, 085108 (2011).
- <sup>19</sup>Z. Warhaft and J. L. Lumley, “An experimental study of the decay of temperature fluctuations in grid-generated turbulence,” *Journal of Fluid Mechanics* **88**, 659–684 (1978).
- <sup>20</sup>K. R. Sreenivasan, S. Tavoularis, R. Henry, and S. Corrsin, “Temperature fluctuations and scales in grid-generated turbulence,” *Journal of Fluid Mechanics* **100**, 597–621 (1980).
- <sup>21</sup>T. Zhou, R. A. Antonia, L. Danaïla, and F. Anselmet, “Transport equations for the mean energy and temperature dissipation rates in grid turbulence,” *Experiments in Fluids* **28**, 143–151 (2000).
- <sup>22</sup>T. Tamura and T. Miyagi, “The effect of turbulence on aerodynamic forces on a square cylinder with various corner shapes,” *Journal of Wind Engineering and Industrial Aerodynamics* **83**, 135–145 (1999).
- <sup>23</sup>G. Vita, H. Hemida, T. Andrienne, and C. C. Baniotopoulos, “Generating atmospheric turbulence using passive grids in an expansion test section of a wind tunnel,” *Journal of Wind Engineering and Industrial Aerodynamics* **178**, 91–104 (2018).
- <sup>24</sup>G. K. Batchelor, “Kolmogoroff’s theory of locally isotropic turbulence,” in *Mathematical Proceedings of the Cambridge Philosophical Society*, Vol. 43 (Cambridge University Press, 1947) pp. 533–559.
- <sup>25</sup>G. K. Batchelor and A. A. Townsend, “Decay of vorticity in isotropic turbulence,” *Proceedings of the Royal Society of London. Series A. Mathematical and Physical Sciences* **190**, 534–550 (1947).
- <sup>26</sup>G. K. Batchelor, “Energy decay and self-preserving correlation functions in isotropic turbulence,” *Quarterly of Applied Mathematics* **6**, 97–116 (1948).
- <sup>27</sup>M. S. Mohamed and J. C. LaRue, “The decay power law in grid-generated turbulence,” *Journal of Fluid Mechanics* **219**, 195–214 (1990).

- <sup>28</sup>P. Lavoie, P. Burattini, L. Djenidi, and R. A. Antonia, “Effect of initial conditions on decaying grid turbulence at low  $R_\lambda$ ,” *Experiments in Fluids* **39**, 865–874 (2005).
- <sup>29</sup>P. Lavoie, L. Djenidi, and R. A. Antonia, “Effects of initial conditions in decaying turbulence generated by passive grids,” *Journal of Fluid Mechanics* **585**, 395 (2007).
- <sup>30</sup>T. Kurian and J. Fransson, “Grid-generated turbulence revisited,” *Fluid Dynamics Research* **41**, 021403 (2009).
- <sup>31</sup>L. Djenidi, M. Kamruzzaman, and R. A. Antonia, “Power-law exponent in the transition period of decay in grid turbulence,” *Journal of Fluid Mechanics* **779**, 544 (2015).
- <sup>32</sup>L. Djenidi, “Lattice-Boltzmann simulation of grid-generated turbulence,” *Journal of Fluid Mechanics* **552**, 13 (2006).
- <sup>33</sup>K. Nagata, H. Suzuki, Y. Sakai, T. Hayase, and T. Kubo, “Direct numerical simulation of turbulent mixing in grid-generated turbulence,” *Physica Scripta* **2008**, 014054 (2008).
- <sup>34</sup>Ö. Ertunç, N. Özyilmaz, H. Lienhart, F. Durst, and K. Beronov, “Homogeneity of turbulence generated by static-grid structures,” *Journal of Fluid Mechanics* **654**, 473 (2010).
- <sup>35</sup>S. Laizet and J. C. Vassilicos, “DNS of fractal-generated turbulence,” *Flow, Turbulence and Combustion* **87**, 673–705 (2011).
- <sup>36</sup>H. Suzuki, K. Nagata, Y. Sakai, T. Hayase, Y. Hasegawa, and T. Ushijima, “Direct numerical simulation of fractal-generated turbulence,” *Fluid Dynamics Research* **45**, 061409 (2013).
- <sup>37</sup>S. Laizet, J. Nedić, and C. Vassilicos, “Influence of the spatial resolution on fine-scale features in dns of turbulence generated by a single square grid,” *International Journal of Computational Fluid Dynamics* **29**, 286–302 (2015).
- <sup>38</sup>R. A. Antonia and P. Orlandi, “Similarity of decaying isotropic turbulence with a passive scalar,” *Journal of Fluid Mechanics* **505**, 123 (2004).
- <sup>39</sup>S. Olivieri, *Elastically-bounded flapping plates for flow-induced energy harvesting*, Ph.D. thesis, University of Genova (2020).
- <sup>40</sup>W.-X. Huang and H. J. Sung, “Three-dimensional simulation of a flapping flag in a uniform flow,” *Journal of Fluid Mechanics* **653**, 301 (2010).
- <sup>41</sup>Y. Xia, S. Michelin, and O. Doaré, “Fluid-solid-electric lock-in of energy-harvesting piezoelectric flags,” *Physical Review Applied* **3**, 014009 (2015).
- <sup>42</sup>F.-B. Tian, H. Dai, H. Luo, J. F. Doyle, and B. Rousseau, “Fluid–structure interaction involving large deformations: 3D simulations and applications to biological systems,” *Journal of Computational Physics* **258**, 451–469 (2014).

- <sup>43</sup>I. Lee and H. Choi, “A discrete-forcing immersed boundary method for the fluid–structure interaction of an elastic slender body,” *Journal of Computational Physics* **280**, 529–546 (2015).
- <sup>44</sup>M. D. de Tullio and G. Pascazio, “A moving-least-squares immersed boundary method for simulating the fluid–structure interaction of elastic bodies with arbitrary thickness,” *Journal of Computational Physics* **325**, 201–225 (2016).
- <sup>45</sup>X. Zhu, E. Phillips, V. Spandan, J. Donners, G. Ruetsch, J. Romero, R. Ostilla-Mónico, Y. Yang, D. Lohse, R. Verzicco, M. Fatica, and R. J. Stevens, “AFiD-GPU: a versatile Navier–Stokes solver for wall-bounded turbulent flows on GPU clusters,” *Computer Physics Communications* **229**, 199–210 (2018).
- <sup>46</sup>R. Verzicco and P. Orlandi, “A finite-difference scheme for three-dimensional incompressible flows in cylindrical coordinates,” *Journal of Computational Physics* **123**, 402–414 (1996).
- <sup>47</sup>F. Viola, V. Meschini, and R. Verzicco, “Fluid–Structure-Electrophysiology interaction (FSEI) in the left-heart: a multi-way coupled computational model,” *European Journal of Mechanics-B/Fluids* **79**, 212–232 (2020).
- <sup>48</sup>E. A. Fadlun, R. Verzicco, P. Orlandi, and J. Mohd-Yusof, “Combined immersed-boundary finite-difference methods for three-dimensional complex flow simulations,” *Journal of Computational Physics* **161**, 35–60 (2000).
- <sup>49</sup>M. Vanella and E. Balaras, “A moving-least-squares reconstruction for embedded-boundary formulations,” *Journal of Computational Physics* **228**, 6617–6628 (2009).
- <sup>50</sup>R. Verzicco, J. Mohd-Yusof, P. Orlandi, and D. Haworth, “Large eddy simulation in complex geometric configurations using boundary body forces,” *AIAA Journal* **38**, 427–433 (2000).
- <sup>51</sup>V. Spandan, V. Meschini, R. Ostilla-Mónico, D. Lohse, G. Querzoli, M. D. de Tullio, and R. Verzicco, “A parallel interaction potential approach coupled with the immersed boundary method for fully resolved simulations of deformable interfaces and membranes,” *Journal of Computational Physics* **348**, 567–590 (2017).
- <sup>52</sup>D. A. Fedosov, B. Caswell, and G. E. Karniadakis, “Systematic coarse-graining of spectrin-level red blood cell models,” *Computer Methods in Applied Mechanics and Engineering* **199**, 1937–1948 (2010).
- <sup>53</sup>G. Ruetsch and M. Fatica, *CUDA Fortran for scientists and engineers: best practices for efficient CUDA Fortran programming* (Elsevier, 2013).
- <sup>54</sup>P. Chakraborty, S. Balachandar, and R. J. Adrian, “On the relationships between local vortex identification schemes,” *Journal of Fluid Mechanics* **535**, 189 (2005).

- <sup>55</sup>A. Thormann and C. Meneveau, “Decay of homogeneous, nearly isotropic turbulence behind active fractal grids,” *Physics of Fluids* **26**, 025112 (2014).
- <sup>56</sup>S. B. Pope, *Turbulent flows* (Cambridge University Press, 2000).
- <sup>57</sup>C. Tropea, A. L. Yarin, and J. F. Foss, *Springer Handbook of Experimental Fluid Mechanics* (Springer Science & Business Media, 2007).